Computational Model of Soft Tissues in the Human Upper Airway

J-P. V. Pelteret*[1], B. D. Reddy[1]

[1]*Centre for Research in Computational and Applied Mechanics, University of Cape Town, 5th floor, Menzies Building, Private Bag X3, 7701 Rondebosch, South Africa*

SUMMARY

This paper presents a three-dimensional finite element model of the tongue and surrounding soft tissues with potential application to the study of sleep apnoea and of linguistics and speech therapy. The anatomical data was obtained from the Visible Human Project, and the underlying histological data was also extracted and incorporated into the model. Hyperelastic constitutive models were used to describe the material behaviour, and material incompressibility was accounted for. An active Hill three-element muscle model was used to represent the muscular tissue of the tongue. The neural stimulus for each muscle group was determined through the use of a genetic algorithm-based neural control model. The fundamental behaviour of the tongue under gravitational and breathing-induced loading is investigated. It is demonstrated that, when a time-dependent loading is applied to the tongue, the neural model is able to control the position of the tongue and produce a physiologically realistic response for the genioglossus. Copyright © 2011 John Wiley & Sons, Ltd.

1. INTRODUCTION

The investigation of diseases involving the upper respiratory tract requires a good understanding of the complex interaction between the air flowing through the system and the tissues in the oropharyngeal region. Syndromes such as obstructive sleep apnoea (OSA) exhibit a complex patho-physiology that is difficult to understand completely using current experimental techniques. The understanding of the fundamentals of all aspects of upper airway respiratory mechanics is becoming increasingly important as these and other disorders become more prevalent. To this end, a computational model of the tongue and surrounding tissues in the human upper airway is presented to further the comprehension of the active mechanics of the tissues in the presence of airflow.

Numerous models of the tongue have been developed by the biomechanics community in order to study speech production [1, 2, 3], active muscle kinematics [4, 5, 6, 7, 8], respiratory mechanics

---

*Correspondence to: Email: jppelteret.uct@gmail.com

Prepared using *cnmauth.cls* *[Version: 2010/03/27 v2.00]*

[9, 10], and the patho-physiology of anatomical defects and the effects of surgical interventions [11]. All of these models have in common the ability to describe individual muscle activation that produces motion due to the contraction of particular muscle groups. However, the underlying description of the constitutive models describing muscle contraction, as well as the degree of accuracy to which they capture the complex underlying musculature histology, differ considerably.

Martins et al.[12, 13] describe a muscle model, developed from an energetic viewpoint, that encompasses all of the fundamental properties exhibited by the skeletal muscle out of which the tongue is composed. This description of contraction is decomposed into distinct parts, each of which have been experimentally validated for different muscle groups [14, 15]. The construct of this model is similar to that described by Wilhelms-Tricario[1], as both of these models account in a similar way for the force-length, force velocity and activation properties intrinsic to muscle fibre functioning.

A component that is not satisfied by any of these models is that of the control of the activation function. The tongue is very complex and a number of muscles are used simultaneously to control its movement at any one time. For the most part, the description of dynamic control inputs has been overlooked. It would appear that each of these models requires predefined descriptions for the activation level, or control signal, governing each muscle. Huang et al.[9] took the first steps in addressing this problem in OSA research by correlating the activity in the genioglossus to the surrounding air pressure. This formed a feedback loop that caused the genioglossus to contract when the surrounding air pressure reduced sufficiently to begin to draw the tongue into the throat.

The focus of this research is to describe the development of a model that could be used to model disorders such as OSA. Both the macroscopic anatomy and microscopic histology are captured in detail and the nature of skeletal muscles and other tissues are to be described by realistic constitutive laws. Active muscle contraction is incorporated and is controlled by a neural control model. The neural model accounts for the unpredictable non-linear deformation of muscular tissues due to complex forces, and controls motion in the absence of meaningful experimental data that can be used to describe muscle activation for all muscle groups used to produce *a priori* deformation. Space-and-time-dependent forces are present due to changing posture causing different orientations of gravitational body forces, respiration and airway geometry, causing changes in airway pressure and muscle contraction itself.

2. IMAGING, DATA EXTRACTION AND MODEL CONSTRUCTION

The anatomical dataset used to construct the computational geometry was sourced from the Visible Human Project [16]. Photographs from the female donor, taken at a resolution of $\frac{1}{3}$mm^3, were imported at their full resolution into the commercial software Mimics [17]. Individual anatomical features were extracted using manual segmentation tools, with an emphasis on retaining anatomical accuracy. Figure 1a illustrates the masking process of the body of the tongue, mandible, hyoid, epiglottis and surrounding soft-tissue.

The tongue is a histologically complex organ comprising numerous interwoven muscle groups. Visible in the reconstructed high-resolution data set was the gross directionality of the muscle groups that constitute the body of the tongue. Fibre data for each muscle group was defined in Mimics
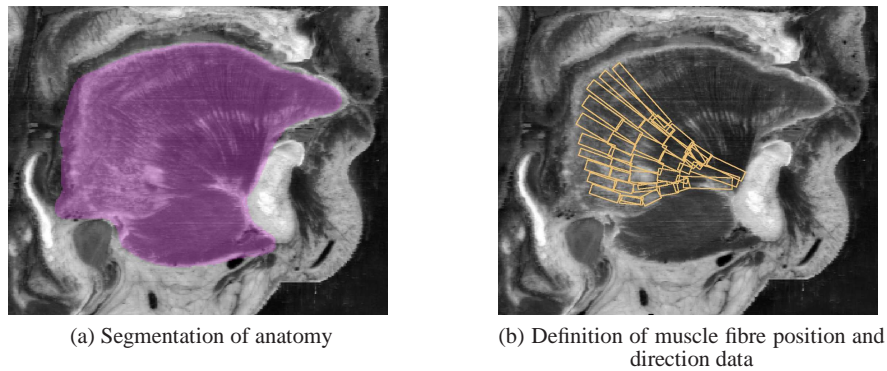
(a) Segmentation of anatomy

(b) Definition of muscle fibre position and direction data

Figure 1. Extraction of anatomical data in Mimics (mid-saggital plane)

by manually selecting regions of each muscle group that had a similar directionality. Figure 1b demonstrates the process in the orientation-definition of fibre bundles for the medial portion of the fan-shaped genioglossus. Here it was assumed that all fibres within each cylindrical bounding box have a similar orientation. Muscle groups that were not highly visible in the photographs were extracted by consulting anatomical literature [18, 19, 20]. A total of 18 unique muscle groups, illustrated in figure 2, with differentiation between left- and right-side muscles, were included. Six of these muscle groups originate from a fixed anatomical structure that is external to the tongue body.
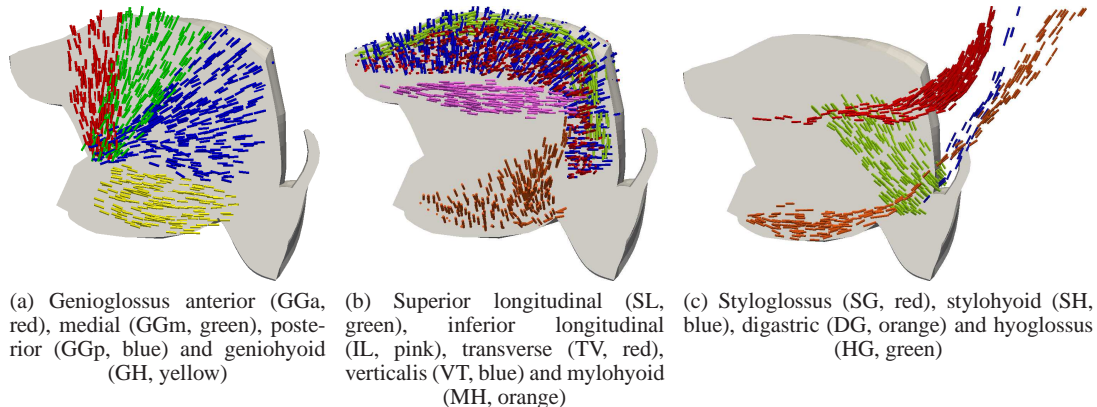

(a) Genioglossus anterior (GGa, red), medial (GGm, green), posterior (GGp, blue) and geniohyoid (GH, yellow)

(b) Superior longitudinal (SL, green), inferior longitudinal (IL, pink), transverse (TV, red), verticalis (VT, blue) and mylohyoid (MH, orange)

(c) Styloglossus (SG, red), stylohyoid (SH, blue), digastric (DG, orange) and hyoglossus (HG, green)

Figure 2. Micro-scale hystological data defined for the image dataset

Anatomical data was subsequently imported into ICEM CFD [21] for surface definition, assembly and meshing. The dataset used is not ideal for this work as, at the time of imaging, the tongue is not in a natural position (it was clamped between the subject's teeth). Due to this, as well as the complexity of the anatomy in histology, shape and part connectivity, minor alterations and simplification were performed to produce a high-quality fully hexahedral model. Literature in human physiology references [18, 19, 20] was again used in order to ensure that the integrity of the model was preserved.

The dataset of the micro-scale fibre directionality was subsequently imported into the macro-scale geometry, providing a perfect match between the two datasets. The genioglossus was represented

by three independently controlled functional units, namely the anterior, medial and posterior components, as discussed by Miyawaki et al.[22] and used elsewhere [23, 4, 7]. Due to the general constitutive framework given in section 3.2, the description of the muscle model described in section 5.2, and the fact that the fibre and anatomical datasets correspond exactly, there was no requirement for the mesh to align with the direction of any of the underlying fibre groups. The underlying muscle histology data was interpolated directly onto the constructed mesh.

3. CONTINUUM MECHANICS

3.1. Kinematics with a zero strain configuration

The non-linear motion φ, mapping points in the reference configuration Ω_0 to points in the current configuration Ω, is defined by $x = \varphi(X, t)$ and the deformation gradient associated with the motion is given by $F = \nabla_X \varphi = I + \nabla_X u$ where the spatial gradient is taken with respect to the material coordinate system.

We account for the pre-strained and pre-stressed configuration of the geometry extracted from the images by defining an additional configuration state, namely the zero-strain configuration.

We choose to define an initial configuration Ω_I that is not necessarily the same as the reference configuration. In order to accomplish this, we redefine the total deformation gradient as

$$F = F_{CR}F_{RI} \tag{1}$$

so that the total deformation gradient is multiplicatively decomposed into two motions with F_{RI} and F_{CR} respectively mapping points from the initial to the reference configurations and the reference to current configurations.

3.2. Constitutive equations for fibrous hyperelastic materials

A strain-energy function (SEF) that governs the behaviour of a general fibrous hyperelastic material is given by [24, 12, 25]

$$\psi = \psi\left(J, \bar{b}, \bar{\lambda}_f\right) = \psi_J(J) + \phi_M\psi_M\left(\bar{I}_1^b, \bar{I}_2^b\right) + \sum_f \phi_f\psi_f\left(\bar{\lambda}_f\right) \tag{2}$$

with the rule of mixtures [26, 27], valid for incompressible materials, applied to describe the volume fractions of the constituent components

$$\phi_M + \sum_f \phi_f = 1 \tag{3}$$

The first term in (2) describes the volumetric response of the material with $J = \det(F)$. The second term describes the isochoric respose of a general bulk material with the description given in terms of invariants of the isochoric part of the left Cauchy-Green tensor $\bar{b} = J^{-\frac{2}{3}}FF^T$. The third term introduces isochoric anisotropic contributions from any fibres that may be embedded in the bulk

material and are dependent on the fibre stretch $\bar{\lambda}_f = \sqrt{\boldsymbol{N}_f \cdot \bar{\boldsymbol{C}} \boldsymbol{N}_f}$, where $\boldsymbol{N}_f$ is the fibre direction defined in the reference configuration.

Note that this formulation allows for the presence of multiple interweaving fibre families at any point in the domain [25]. The bulk material can therefore be one that is isotropic, uniaxially orthotropic, transversely isotropic or completely anisotropic. Fibre families are assumed not to interact with one another through the action of friction or any other direct mechanism. The overall response is, however, coupled.

Since the fibres now have a finite volume, they are required to sustain transverse and shear loads. However, the material model for the fibres describes only the axial loading response of the fibres. It is assumed that the transverse and shear loading response of a fibre bundle is the same as that of the underlying matrix. The overall Kirchhoff stress at any point in the domain is given by [28, 26]

$$\boldsymbol{\tau} = \boldsymbol{\tau}_J (J) + \phi_M \boldsymbol{\tau}_M \left(\bar{I}_1^b, \bar{I}_2^b \right) + \sum_f \phi_f \boldsymbol{\tau}_f \left(\bar{\lambda}_f \right) \tag{4}$$

$$= \boldsymbol{\tau}_J + \boldsymbol{\tau}_M + \sum_f \phi_f \left(\lambda_f \psi_f' - \sum_f \phi_f \left(\boldsymbol{\tau}_M : \boldsymbol{n}_f \otimes \boldsymbol{n}_f \right) \right) \boldsymbol{n}_f \otimes \boldsymbol{n}_f \tag{5}$$

$$\approx \boldsymbol{\tau}_J + \boldsymbol{\tau}_M + \sum_f \phi_f \lambda_f \psi_f' \boldsymbol{n}_f \otimes \boldsymbol{n}_f \tag{6}$$

where (4) gives the stress with a fibre description in the current configuration that can hold transverse and shear loads, and (5) has the transverse and shear loading processed out as described in [26] for multiple fibre families. Since the fibre volume fraction is high and the passive component of muscle fibre is very compliant at low stretch and only resists tensile deformation, this model does not easily describe behaviour representative of the experimentally obtained relationships passive muscular tissue (e.g. [29]) as there is little resistance to deformation in the fibre direction, and no resistance in compression [30]. We therefore choose to keep the matrix stress component in the fibre direction, resulting in (6), which better reproduces the stress-strain relationships observed in the experimental data but introduces an extra stiffness component in the fibre direction under tensile deformation.

4. LINEARISATION AND FINITE ELEMENT IMPLEMENTATION

A three-field functional that describes potential energy in the system is developed [31, 32]. This functional, which exploits the additive split of strain-energy function, is given by

$$\Pi \left(\boldsymbol{\varphi}, \theta, \Lambda, p \right) := \int_\Omega \left\{ \left[\hat{\psi}_{\text{vol}} \left(\theta \right) + \hat{\psi}_{\text{iso}} \left(\bar{\boldsymbol{b}}, \bar{\lambda}_f \right) \right] + p \left(J - \theta \right) + \Lambda \left(\theta - 1 \right) \right\} d\Omega - \Pi \left(\boldsymbol{\varphi} \right)_{\text{ext}} \Rightarrow \text{stationary} \tag{7}$$

where $\hat{\psi}_{\text{vol}}$ is a function of the dilatation, p is a Lagrange multiplier interpreted as the hydrostatic pressure and Λ is a Lagrange multiplier enforcing the incompressibility constraint and $\Pi \left(\boldsymbol{\varphi} \right)_{\text{ext}}$ gives the strain energy due to the influence of external sources. Inertial terms are neglected due to the assumption of slow movement of the anatomy and θ represents the dilatation of the body. However, since the loading conditions are not constant and there are rate-dependent variables in the

muscle model, the problem remains dependent on time but no time discretisation of the governing equations is required.

A robust, stable and computationally efficient formulation that successfully accommodates the requirement for incompressibility is desired. For these reasons, we choose to approximate the displacement field with continuous trilinear shape functions and the pressure and dilatation fields with element-wise constant (discontinuous) functions. The resulting Q1-P0 element, proposed by Nagtegaal et al.[33] and developed by Simo et al.[34] has all of the required characteristics, and alleviates issues of volumetric locking in incompressible materials and shear-locking in bending problems experienced by standard trilinear elements [32].

The finite element method, in conjunction with a Newton-Raphson solution algorithm, implemented using open-source finite-element library `deal.II` [35, 36], is used to solve for the displacement field. Λ is treated as an augmented Lagrange multiplier in order to effectively enforce incompressibility without creating an over-stiff system that is computationally expensive to solve. Use of the Uzawa update scheme [31] allows the Lagrange multiplier to be treated as constant within a Newton-Raphson. Incompressibility is considered to be attained when the overall dilatation error is less than 0.1%.

The discretised system that is formed through the linearisation of (7) and the subsequent spatial discretisation requires the calculation of stress at integration points. This implies that it is necessary to describe the nature of fibre behaviour at these integration points through a material model which accounts for the properties (direction, stretch, activation etc.) of the underlying fibres. The result is that, for internal muscles, the local behaviour of sarcomeres that constitute a part of a muscle fibre in the vicinity of the integration point is represented. For external muscles, a single muscle fibre inserting into a point on the boundary is modelled and assumed to have the same properties throughout its entire length.

The boundary Γ is decomposed into non-overlapping components Γ^{φ} and Γ^{t}. The essential boundary condition $\varphi = \bar{\varphi}$ on Γ^{φ} is imposed on the surfaces with known displacement. The natural boundary condition, imposed on all other surfaces, is $\boldsymbol{t} = \bar{\boldsymbol{t}} = \boldsymbol{\sigma}\boldsymbol{n} + \boldsymbol{t}_f$ on Γ^{t} where $\boldsymbol{\sigma}$ represents external stresses acting on the body, $\boldsymbol{n}$ is the outward normal at the surface of the body and $\boldsymbol{t}_f$ an additional traction described in section 5.2.1. For surfaces that experience the influence of external pressure, $\boldsymbol{\sigma} = -p\boldsymbol{I}$ and free boundaries have no traction, i.e. $\boldsymbol{t} = \boldsymbol{0}$.

5. CONSTITUTIVE MODELS

5.1. Bone, cartilage, adipose tissue

For the loading conditions considered, the hard tissues are expected to undergo significantly less deformation than soft tissues. Both bone and cartilage are considerably stiffer materials in comparison to the muscle and adipose tissue. For this reason a simple Neo-Hookean model

$$\psi_{\mathrm{hard}} = C_1 \left(I_1^b - 3 \right) \quad , \quad C_1 = \frac{\mu}{2} \quad , \tag{8}$$

where $\mu = E/(2(1 + \nu))$ is the shear modulus with E and ν the Young's modulus and Poisson's ratio respectively, is adopted as it is able to capture the small strain nature of their deformation adequately.

A Fung free-energy function, representative of many biological materials, was used to describe the behaviour of the adipose tissue. Adipose tissue exhibits viscoelastic effects [37], which have been ignored for simplicity. The SEF that describes the adipose tissue is

$$\psi_{\text{adip}} = A_1 \left(e^{B_1 \left(I_1^b - 3 \right)} - 1 \right) \quad , \tag{9}$$

with A_1 and B_1 representing material parameters.

5.2. Muscle model

There are two facets to modelling muscles that need careful consideration: the constitutive relationships governing the material behaviour, and the signals to the muscle that control its contractile behaviour. This section focuses on the former issue, while section 6 deals with the latter.

Muscle tissue is composed of a largely homogeneous and isotropic bed matrix in which muscle fibres are embedded. Each group of muscle fibres is made up of several sub-units, of which the smallest functional unit is the sarcomere. Figure 3 depicts the arrangements of the sarcomeres in a muscle fibre. By assuming that in a small control volume all sarcomeres belonging to a fibre family behave identically, one can describe the local motion of the fibre by describing the motion of a single sarcomere.
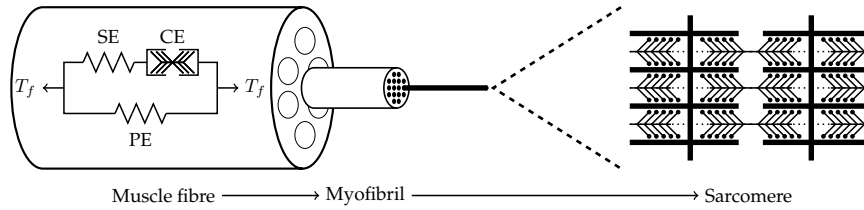

Figure 3. Physiology of a skeletal muscle fibre: Macro-scale (muscle fibre) to micro-scale (sarcomere). The Hill three-element model, overlaid on a muscle fibre, represents the behaviour of a collection of sarcomeres. The parallel (PE) and series (SE) elements are passive and the contractile element (CE) is responsible for the active reduction of muscle length.

No restriction is placed on the number of muscle fibre families present at each point in the muscle. This allows for the notion of crossing and interweaving muscle groups, a histological feature found in the tongue. Adjacent fibre families are assumed to slide over each other, so no cross-terms and direct interaction are modelled in the constitutive equations.

Martins et al.[12, 13] consider the muscle matrix to be a Fung-type hyperelastic material with a exponential stress-strain relationship, given by

$$\psi_M = c \left(e^{b \left(I_1^b - 3 \right)} - 1 \right) \quad . \tag{10}$$

The density of the muscle matrix is set at $\rho = 1060$ kg/m^3. The parameters for the muscle matrix, given in table I, were chosen such that Young's modulus at zero strain and high strain,

as approximated under uniaxial tension conditions, would be within the range of values described in the literature [2, 29, 4, 38, 39, 9, 30, 5, 7].

The Hill three-element model, shown in figure 3 and described by [40], is a representation of muscle at a sarcomere level. Each of the elements represent a collection of different physical components of the sarcomere. The material behaviour of muscle fibres is described in terms of a general, but undefined SEF ψ_f that is dependent on the stretch in the fibre direction. The resulting equation for stress, (6), involves the derivative of the SEF with respect to the fibre stretch; this term is interpreted as the one-dimensional tensile force in the muscle fibre as described in (11).

Histology samples of the tongue musculature [41, 42] depict the tongue as being a densely fibrous body. The fibre volume fraction of skeletal muscle has been measured to a value as high as 0.95 [43], although the volume fraction of fat in the tongue has been experimentally determined to be approximately 0.25 [44] and the fraction of muscle fibres plus connective tissue in the tongue has been measured in the range of 0.44–0.64 [45]. A more conservative value of 0.7 was chosen for the total fibre fraction, with this value being equally split between each fibre family that occupies a certain position in space.

Using the Hill three-element model, the total force in the muscle fibre can be additively decomposed into the sum of the tension in the parallel and series element: that is,

$$\psi_f'\left(\lambda_f\right) = T_f = T_f^p\left(\lambda_f\right) + T_f^s\left(\lambda_f, \lambda_c\right) \quad , \tag{11}$$

with the additional relationship that the series and contractile tension are equal:

$$T_f^s\left(\lambda_f, \lambda_c\right) = T_f^c\left(\lambda_c, \dot{\lambda}_c, \alpha\right) \quad . \tag{12}$$

In [13], a multiplicative split of the contractile and series strain is assumed; that is, the total fibre stretch in the two-element branch can be described as a composition of the stretch of the series element superimposed on that of the contractile element:

$$\lambda_f = \lambda_s \lambda_c \quad . \tag{13}$$

The local equilibrium relationship in (12) and stretch relationship in (13) are used to solve for λ_c at each outer Newton-iteration for a constant λ_f. A hybrid bisection-Newton method [46] is used for stability purposes as the relationships describing the contractile element are highly non-linear and, under certain circumstances, highly sensitive to perturbations.

The above-mentioned relationships are presented in detail in equations (14)–(16). Martins et al.[13] describe the force in each element in terms of $T_0^{\max}$, the maximum tensile force that can be attained in the element, and experimentally determined scaling functions, by

$$T_f^p\left(\lambda_f\right) = T_0^{\max} f_p\left(\lambda_f\right) \quad , \tag{14}$$

$$T_f^s\left(\lambda_f, \lambda_c\right) = T_0^{\max} f_s\left(\lambda_f, \lambda_c\right) \quad , \tag{15}$$

$$T_f^c\left(\lambda_c, \dot{\lambda}_c, \alpha\right) = T_0^s T_0^{\max} f_c^L\left(\lambda_c\right) f_c^V\left(\dot{\lambda}_c\right) \alpha\left(u\left(t\right)\right) \quad , \tag{16}$$

with $T_0^{\max}$ representing the peak isometric stress that can be attained in the muscle and the additional factor of T_0^s is motivated in section 6.

The parallel element representing the connective tissue and collagenous sheaths surrounding the fibre have an exponential constitutive law [47, 13]

$$
f_p\left(\lambda_f\right) = \begin{cases} 2aA\left(\lambda_f - 1\right)e^{a\left(\lambda_f - 1\right)^2} & \text{if} \quad \lambda_f > 1 \\ 0 & \text{if} \quad \lambda_f \leqslant 1 \end{cases} . \tag{17}
$$

The intrinsic elastic properties internal to the sarcomere are represented by the series element. It also has an exponential stretch-tension relationship [47] described by [13]

$$
f_s\left(\lambda_f, \lambda_c\right) = \begin{cases} c_1\left(e^{c_2\left(\lambda_f - \lambda_c\right)} - 1\right) & \text{if} \quad \lambda_s > 1 \\ 0 & \lambda_s \leqslant 1 \end{cases} . \tag{18}
$$

It should be noted that both the parallel and series elements function only in tension. Parameters for the parallel and series elements are given in table I.

Table I. Muscle material parameters: Muscle matrix, fibres, PE, SE

Parameter	Matrix		Fibre		PE f_p	SE f_s		
	b	c	ϕ_f	$T_0^{\max}$	a	A	c_1	c_2
Units	–	kN/m^2	–	kN/m^2	–	–	–	–
Value	0.6265	1.652	0.7	668.8	8.568×10^{-4}	12.43	0.1	100

The contractile element has a dependence on its stretch, rate of stretch and the level of activation of the muscle. The force-length and force-velocity relationships are well defined in the literature e.g. [48, 40, 49, 14, 15], but exhibit discontinuous behaviour. In order to overcome this, Gaussian-type mollifier functions are proposed; these match the experimental data closely while being infinitely differentiable functions and easier to use in algorithms. The length and velocity dependent functions for the CE are described by

$$
f_c^L\left(\lambda_c\right) = \begin{cases} \sum_{n_L} g_n\left(\lambda_c\right) & \text{if} \quad 0.5 < \lambda_c < 2 \\ 0 & \text{otherwise} \end{cases} \tag{19}
$$

$$
f_c^V\left(\dot{\lambda}_c\right) = \begin{cases} 0 & \text{if} \quad \dot{\lambda}_c \leqslant -10 \\ \sum_{n_V} g_n\left(\dot{\lambda}_c\right) & \text{if} \quad -10 < \dot{\lambda}_c < 0.5 \\ 1.5 & \text{otherwise} \end{cases}, \tag{20}
$$

with the contractile velocity $\dot{\lambda}_c$ calculated using a backward Euler method, and the Gauss-mollifier function is defined as

$$
g_n\left(x\right) = \underbrace{\left(A_n e^{-B_n\left(x - \mu_n\right)^{p_n}}\right)}_{\text{Gauss function}} \underbrace{\left(\left[x - \mu_n\right]^{q_n} - R_n^{q_n}\right)^{s_n}}_{\text{Cutoff function}} . \tag{21}
$$

In (21) the terms in the first bracket define the shape of the curve in most of the region of interest, while the terms in the second bracket forces the function towards zero at a selected radius from a chosen epicentre so that the function is closed.

Table II. Muscle material parameters: CE

n	CE f_c^L			CE f_c^V				
	1	2	3	1	2	3	4	5
μ	0.8	1.3	1.325	-0.75	-0.6	0.55	1.4	0.75
p	2	2	1	2	2	2	4	8
A	0.475	0.100	4830.635	2.5×10^{-5}	0.3	0.425	0.1	0.525
B	90	10	3	0.01	0.25	0.7	0.3	15
R	1	1	0.75	10	0	0	0	0
q	4	2	4	2	0	0	0	0
s	8	8	8	2	0	0	0	0

Table II lists the parameter values used in the above equations. These parameters were tuned according to data and functions described in literature. Figure 4a illustrates the correlation of (19) to force-length data described in [14], while figure 4b shows the degree to which (20) matches data from [15].
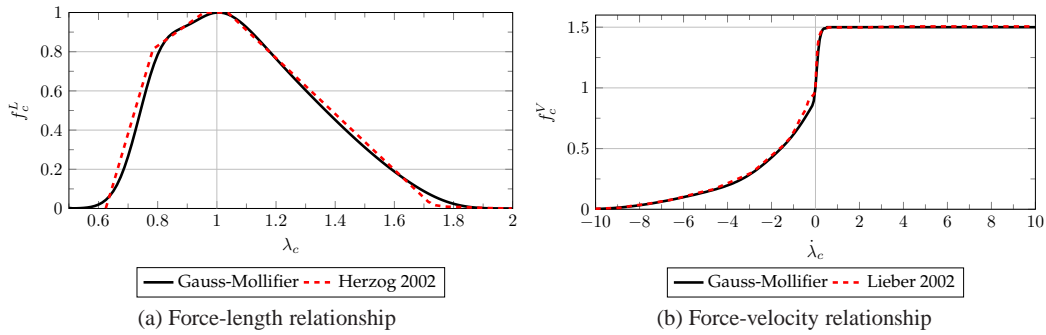

(a) Force-length relationship (b) Force-velocity relationship

Figure 4. CE length, velocity relationships

5.2.1. Action of external muscles

The tongue uses not only internal muscles to perform complex movement, but makes use of external muscles as well. These muscles have a point of origin outside the tongue where they are attached to a bony fixture point and insert and terminate inside the tongue. Direct inclusion of these external models into a computational model is difficult as the geometry of the external muscles and the tissue that surround them are hard to define. However, it is possible to include their effect indirectly using a simplified model of these muscles.

We define the point of origin $\boldsymbol{P}_0^O$ of the external muscle and a general point of insertion $\boldsymbol{P}^I(\boldsymbol{\varphi})$ into the tongue. The origin is considered a fixed point in space and time, while the insertion points for a collection of fibres define a complex surface on the boundary of the tongue with a non-zero cross-sectional area. The fibre direction and length can be calculated from this vector

$$L_f \boldsymbol{n}_f = \boldsymbol{P}_0^O - \boldsymbol{P}^I \quad . \tag{22}$$

Noting that the fibre stretch is simply $\lambda_f^E = L_f/L_f^0$, the nominal stress in the fibre can be calculated using equations (11) and (14)–(16).

Since these muscles insert into the bulk region of the tongue, the portion of the muscles that are within the tongue are treated as internal fibres but these internal and external muscles collectively define the muscle group. The insertion region on the boundary on which the muscles act define the interface where the external fibres transition to internal fibres. The action of external muscle groups are incorporated into the geometry through the traction boundary condition given by

$$t_f = \phi_f \lambda_f T_f n_f \quad . \tag{23}$$

The volume fraction of the external portion of these muscles is that given in table I and value of t_f is displacement dependent and is consistently linearised to maintain the stability of the algorithm.

6. MUSCLE ACTIVATION AND NEURAL MODEL

The contractile element is an active element, so the contractile stress developed by the element, as defined by (16), is related to the level of activation α_M in each muscle group M. The activation level is dependent on the electrical stimulus sent to the muscle.

Pandy et al.[50] present a time-dependent ordinary differential equation, which approximates the activation function under simplified conditions. This is defined, for each muscle M, by

$$\dot{\alpha}(t) = \frac{1}{\tau_R}[1 - \alpha]u + \frac{1}{\tau_F}[\alpha_{\min} - \alpha][1 - u] \tag{24}$$

where α is the muscle activation level, $\alpha_{\min}$ is the minimum muscle activation level and $u = u(t) = \{0, 1\}$ is the net neural control signal to the muscle. With the chosen parameters, the zero-strain stiffness of the matrix model accounts for the resting muscle tone [7], thus the appropriate value of $\alpha_{\min}$ is zero. This description of muscle activation does not account for the differing degrees of muscle contraction determined by signal frequency. (24) is solved using a backward Euler method. Section 6.1 discusses the neural input, u, to each muscle family. The activation rise and fall rates for the genioglossus, set at $\tau_R = \tau_F = 150$ms, were chosen to match integrated EMG data obtained during free respiration [51, 52, 53] assuming a maximum activation level of unity, and were carried over to other muscle groups in the absence of data in the literature.

Regular motions of the tongue do not require extreme forces to be generated in the muscles in order to produce them, as demonstrated in section 8.4. The state of contraction of the muscle depends on the frequency of the electrical impulse transmitted to the muscle [40]. Since the contraction model collectively described by [13] and [50] does not cater for this concept, we decompose the peak contractile stress into two components, namely $T_0^c = T_0^s \, T_0^{\max}$. Now $T_0^{\max}$ is the absolute maximum isometric stress that can be produced by the muscle and $T_0^s \in [0, 1]$ is a scaling factor that reduces the maximum contractile stress that can be developed.

The product of T_0^s and the muscle activation level describe the degree of contraction as a fraction of the full muscle response (FFMR = $T_0^s \alpha$). With these parameters, three noteworthy cases can arise:

1. $T_0^s = 1, \alpha = 1$: The muscle is producing the maximum contractile stress.

2. $T_0^s < 1, \alpha = 1$: The muscle is fully activated at a lower impulse frequency.
3. $T_0^s \leqslant 1, \alpha < 1$: The muscle has not yet developed a maximum allowable state of contraction.

By altering the values of T_0^s, τ_R and τ_F, more precise control of movement is developed by the neural model.

6.1. Control of neural input signals

During a cycle of inhalation and exhalation, the airway pressure drops and distorts the soft tissue of the oropharynx thereby altering the airflow within the upper airway. In response to this, various muscle groups contact in order to prevent movement of the tissue and the subsequent blockage of the airway tract. During the act of breathing, the tongue is kept forward and down in the mouth primarily through the action of the genioglossus. A very distinct pattern of electrical activity is observed in EMG readings of the genioglossus during a respiratory cycle [51, 52, 53, 54]. In a healthy subject the tongue is kept in roughly the same position throughout the respiratory cycle by this autonomic muscle contraction – Cheng et al.[55] observed a posterior displacement of less than 2 mm on the distal surface of the tongue during respiration.

We explored mimicking the proprioceptive capabilities of the tongue by capturing information regarding the current three-dimensional position of surface of the tongue in relation to the desired position of those points. The resulting motion is dependent on the action of the muscles whose selection is variable, and seemingly a consequence of the current orientation of the tongue. Proprioception thus would assist in the tongue predicting the consequence of muscle activation before it is performed and thus precisely controlling the motion of the tongue through space.

The objective function that defines this motion (or lack there of) is

$$\min \sum_p \left\| w_p \left(\boldsymbol{x}_p - \boldsymbol{x}_p^* \right) \right\| \tag{25}$$

which defines the distance of some point p away from its goal position, scaled by a weighting factor. The weighting factor introduces a method to place greater significance on the accuracy of some points over others. For all the cases described in this work, $w_p = 1$ for all control points.

For this problem in particular, (25) is specified such that a number of points on the surface of the tongue are to remain as close to their original position as possible, i.e. we seek position maintenance. The ten selected points were at the apex of the tongue, on the superior surface of the tongue (both at the intersection of the posterior and superior surface and half-way between the posterior surface and apex), and half-way up the posterior surface of the tongue. The points were monitored on the mid-saggital line, as well lateral to the midplane. These control points thus form a coarse net defining the superior and posterior surfaces of the tongue.

A number of strategies can be employed to minimise such a function. Genetic algorithms [56, 57], which mimic the evolutionary processes of selection and recombination to probe a search space for the optimum combination of input parameters to minimise a selected function [57]. For this study, a customised genetic algorithm (GA) was implemented using the open-source library *GAlib* [58]. A non-deterministic elitist GA was used to predict a set of neural input signals $\{\boldsymbol{u}\}$ such that (25) is minimised at all evaluation time-steps. Evaluation of the objective function requires solving the global displacement problem for the given neural input signals and determination of

the actual displacement of the control points. As the evaluation process is a costly procedure, minimisation of the solution search space is ideal. To reduce the size of the search space, certain muscle groups are excluded for evaluation based on their length-weighted average fibre stretch $\bar{\bar{\lambda}}_f = \sum_f \lambda_f L_f \big/ \sum_f L_f$ at the current time versus that in the pre-strained reference configuration $\bar{\bar{\lambda}}_f^0$. This evaluates which muscle groups are in a overall tensile state and through which contraction may assist in returning the tongue to its original position. The local fibre length L_f is approximated from the computational cell geometry and the fibre orientation. The components of the genioglossus are excluded from this selection procedure and are all evaluated at each GA cycle. In the initial population, all corners of the solution space and a prediction for the solution based on previous steps are evaluated.

7. ILLUSTRATIVE EXAMPLES

7.1. Muscle model

To illustrate the functioning of the muscle and neural models, a simple problem setup is used. A block of incompressible muscle tissue of size $1 \times 1 \times 1$ mm^3, with one vertex at the origin, has a planar motion constraint on the coordinate planes. The other three sides are nominally traction-free. Three orthogonal internal muscle families are embedded, each aligned with a coordinate direction, and an external muscle that inserts into the positive y surface of the block from an origin 2 mm away from the surface. The origin of each external fibre is governed by a spacing rule

$$P_0^O = c_s \, P_0^I \ , \ \ P_1^O = h + P_1^I \ , \ \ P_2^O = c_s \, P_2^I \tag{26}$$

with $h = 2$ mm the height above the surface and c_s a spacing constant that controls the angle of insertion (AOI) of the fibre into the surface. The basic geometry is shown in figure 5a. For all cases, the block was discretised into 8^3 equally sized cells. The time-step size was 5ms, with a cumulative time of 500ms, and the activation parameters $\tau_R = \tau_F = 150$ms and $T_0^s = 0.1$ for all active muscle groups.

To demonstrate the basic functioning of the muscle model, three scenarios with prescribed activation histories and no applied traction are simulated. In the first, only the e_1 and e_3 aligned fibres are activated by setting $u_M = 1$ while in the second and third, only the external muscle is contracted. In the second case, the AOI of the fibres to the surface is made very small by setting $c_s = 1$, while in the third $c_s = 2$, resulting in a significant AOI.

The result of the three muscle configurations is shown in figures 5b–5d. In the first case, a the block displaces in the positive Y direction due to the simultaneous activation of the transverse orthogonal muscle groups and the incompressible nature of the material. In the second and third cases, a similar result is achieved due to the contraction of the external muscle. For the third case, the lateral displacement of the upper surface is substantially larger than the second due to the greater AOI. It was observed that the final contractile stress distribution in the external fibres is less uniform as the AOI increases due to the muscle force-length relationship.
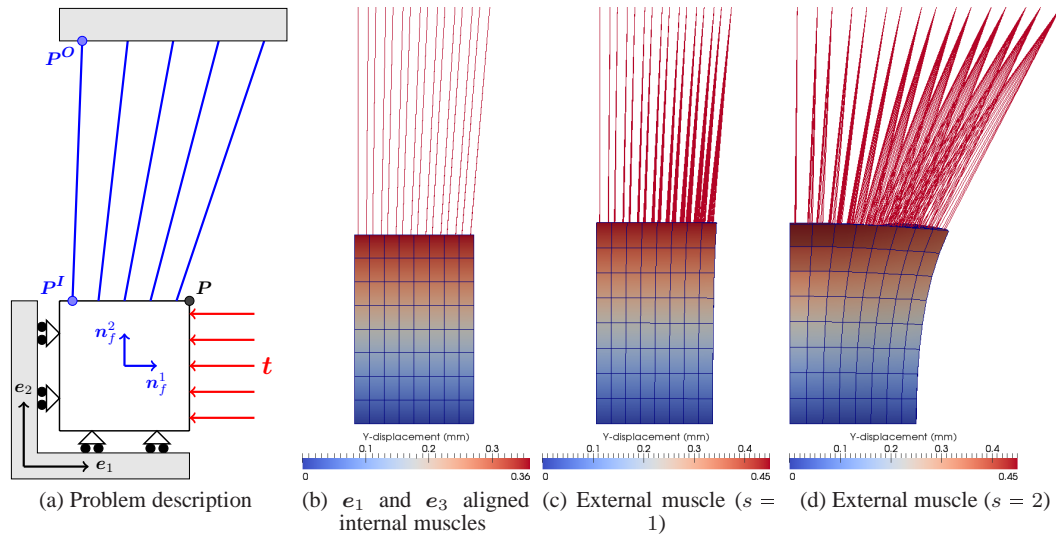
| (a) Problem description | (b) e_1 and e_3 aligned internal muscles | (c) External muscle ($s = 1$) | (d) External muscle ($s = 2$) |

Figure 5. Example problem description: A 1mm^3 block of muscle tissue with deformation controlled by manual activation of the specified muscle groups. Results are shown at $t = 500$ ms for the contraction of the specified muscle groups.

7.2. Neural control model

To demonstrate the capabilities and shortcomings of the genetic algorithm approach, two illustrative examples based on the problem demonstrated in section 7.1 are presented and discussed. In both instances, a compressive pressure load described by

$$p = p_{\max} \left(\sin \omega t\right)^{1.75} \quad , \quad \omega = \frac{2\pi}{2.5} \tag{27}$$

with $p_{\max} = 5000$ Pa and is applied to the side faces of the block. The objective function, given by (25), is that under the action of muscle contraction four control points located on the corners of the positive y-face remain in their reference position. We choose to monitor the point $P = (1, 1, 1)$ mm on the corner of upper surface and the two specified-traction surfaces. All muscle groups are allowed to activate as necessary in order to prevent motion of the upper surface.

In figure 6a, the applied pressure as well as the evolution of the distance that of corner P from the expected equilibrium position for both cases, as well for when position control is not imposed, is shown. In the passive case, where the loading causes an extension in direction e_2 and compression in e_1 and e_3, only the matrix and PE of the e_2 orientated fibres provide resistance to deformation. Comparison of the passive and active cases demonstrates that the genetic algorithm is able to maintain the position of P close to its goal position.

The muscle contraction history for the internal muscle groups is shown in figure 6b. A cyclic response, coinciding with the regularly changing traction load, is present in each muscle group. At the start of each cycle, the e_2 fibre contracts to oppose the motion generated by the load. However, since control of the developed contractile stress is limited, the e_1 and e_3 co-contract to oppose the excessive force generated in the e_2 fibres – this balance is maintained throughout the cycle. Towards the middle of the cycle, where the load is at a maximum, the e_1 and e_3 muscles deactivate and the e_2 muscle attains a maximum activation level. As the load decreases, a similar activation pattern seen

(a) Total displacement of $\boldsymbol{P}$

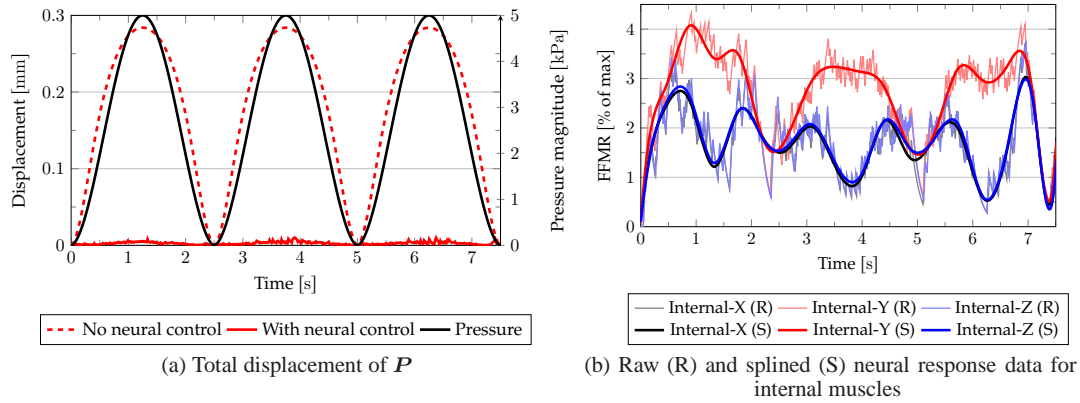(b) Raw (R) and splined (S) neural response data for internal muscles

Figure 6. Block with sinusoidal pressure load. The maximum applied pressure was +5000 Pa and $T_0^s = 0.05$ for all muscles. The external muscle did not attain a significant activation response and is thus not shown in the results.

in the beginning of the cycle is present to provide fine position control. At the end of each cycle, the activation levels of all muscles are non-zero but equal, locking the cube in its original configuration.

This example demonstrates that the neural model functions as expected. However, the model is reactive to its current state and not predictive in a way that truly mimics the motion control exhibited in the body. It has been observed that, although the results are not repeatable due to the random nature of the GA, the trends in the results are repeatable, as demonstrated here and in section 8.5.

8. UPPER AIRWAY TISSUE MODEL

The results of various aspects of the study are presented and discussed in this section.

The tissue material parameters used in the model are as follows: Bone is assumed to have a Young's modulus of 15 GPa [59], Poisson's ratio of 0.4 [60] and density of 1900 kg/m^3. For the cartilage of the epiglottis, the zero-strain elastic modulus was assumed to be 3 MPa for the slow load changes exerted on the tissue [59] and a Poisson's ratio of 0.42 [61]. The density of the cartilage was assumed to be 1000 kg/m^3 as it is comprised mainly of water. Adipose tissue, described by (9), takes the parameters $A_1 = 2500$ Pa and $B_1 = 2.75$, chosen to fit uniaxial compression test data for the plantar region of the foot [62] and a density of 920 kg/m^3 [63]. The parameters for the muscle model are as given in tables I, II and the activation level parameters given in section 6.

The mandible is considered rigid and fixed in space. A zero-displacement condition is imposed on the surface describing the interface between the adipose tissue and the thyroid cartilage to which it is attached. The remaining surfaces have a zero or predefined traction condition.

8.1. Pre-strain, pre-stress condition

Due to the presence of a body force, the body configuration reconstructed from the imaging data is not stress-free. To account for this, we define the initial configuration to be one which when under the influence of gravity, with the loading corresponding to a person standing in the upright position, results in the configuration defined by the reference configuration. Under more complex

circumstances, there is a need to solve for the zero-strain configuration iteratively [64]. However, since the cadaver was orientated in an upright position when the images were taken, a known and simply described loading force acted on the body during imaging.
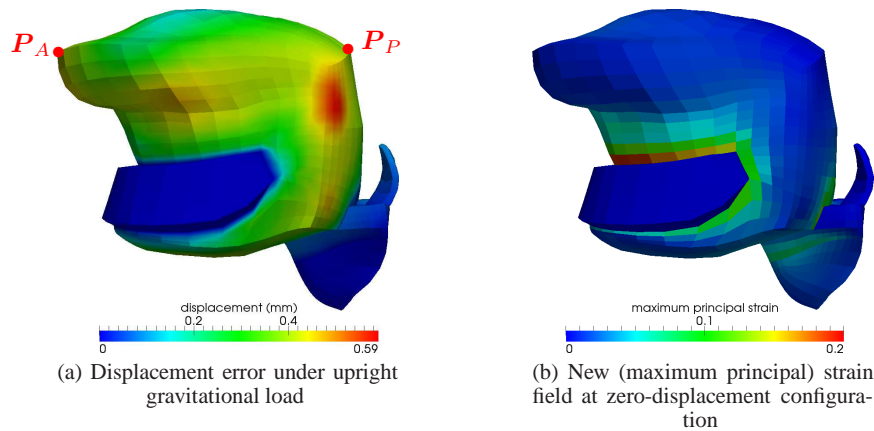

(a) Displacement error under upright gravitational load

(b) New (maximum principal) strain field at zero-displacement configuration

Figure 7. Pre-straining ensures that under upright gravitational loading that while the body returns to the reference position, the resulting strain is significant.

As a first approximation, a spatially constant body force with a magnitude equal to 1.2 times that of gravity is applied in a direction opposite to the natural gravitational direction and assume that this configuration is the zero-strain configuration. It was observed that when reapplying the gravitational force in the upright orientation (that experienced by the cadaver during imaging), the resulting displacement away from the reference configuration was minimal, as depicted in figure 7. The small final displacement indicated that this is a sufficiently accurate approximation for the zero-strain configuration for the purpose of this work. The small displacement is present primarily as a result of the non-linearity of the material behaviour.

8.2. Mesh dependence study

A basic mesh-dependence study was performed to determine the appropriate element density required for the production of satisfactory model results. Three variations of the same model were used with varying element counts in each part, as described in table III. In each model, the number of elements in the tongue were increased roughly by a factor of two. The results of the model with the highest element count were used as a basis from which to measure the performance of the other models.

Table III. Mesh dependence study: Element count per part

Mesh density	Mandible	Hyoid	Tongue	Adipose	Epiglottis	Total	Ratio (total)
Coarse	128	156	4526	2332	522	7664	1
Medium	220	288	9078	4188	774	14548	1.90
Fine	360	360	18196	6620	1200	26736	3.49

The results of the analysis are given in table IV and figure 7a specifies the position of measurement points discussed below. Due to the reasonably low displacement error margin between the coarse and benchmark model, and that result trends rather than absolute measures are of interest, the coarsest

model was considered satisfactory for use. The major benefit of this model was the computational time saved by using a model with a quarter of the number of element to compared to the finest model.

Table IV. Mesh dependence study: Relative error of total displacement for passive tongue under gravitational and pressure load. Error measure calculated as $E = \left| \boldsymbol{P}_i - \boldsymbol{P}_i^{\mathrm{FINE}} \right| \big/ \left| \boldsymbol{P}_i^{\mathrm{FINE}} \right|$.

Mesh density	CPU time	Gravity		Gravity and pressure	
		$\boldsymbol{P}_A$	$\boldsymbol{P}_P$	$\boldsymbol{P}_A$	$\boldsymbol{P}_P$
Coarse	0.21	-6.77%	-5.35%	-6.55%	-5.21%
Medium	0.45	-3.90%	-2.96%	-3.80%	-2.93%

8.3. Effect of orientation and airway pressure on motion of passive body

An investigation was performed to determine the effect of the orientation of gravity as well as pressure loading on the passive tongue. As there is an assumption of quasi-static motion and there are no time-dependent history variables that influence the material characteristics, time is viewed as a non-dimensional entity. For the first half of the loading $t \in [0, 0.5]$, body force loading is ramped from zero to a maximum value with zero external load, and from $t \in (0.5, 1]$ a linear increase of the traction loading occurs while the body force remains at a constant maximum value. During respiration, the air pressure in the oropharynx falls below ambient pressure as the lungs expand – this drop in pressure is referred to as an increase in negative air pressure. As a coarse representation of the pressure distribution present in the oropharynx during breathing, the nominal pressure load $p_{\max}(\boldsymbol{x})$ is one-dimensional in space with a linear variation from front (point $\boldsymbol{P}_A$) to rear (point $\boldsymbol{P}_P$) and constant in the transverse plane. At $\boldsymbol{P}_A$, the pressure is always 0 Pa while the minimum value of airway pressure at $\boldsymbol{P}_P$ was $p = p_{\max} = -500$ Pa.

The final displaced configuration of the tongue experiencing negative 500 Pa pressure loading under different gravitational loading conditions is shown in figure 8. With no applied load, the tongue remains in a neutral position when gravity is orientated in the upright direction, while the supine orientation causes the tongue to move in the posterior direction. In both cases the influence of pressure ensures that the tongue is drawn backwards towards the posterior region of the oral cavity. It is noted that in all cases, due to both pre-stressing and loading, the spatial variation of local fibre stretch substantial with some regions of the genioglossus, depicted in figure 8, in compression and others in tension.

In figure 9, the measure of overall muscle stretch described in section 6.1 is shown for increasing gravitational and pressure load. It is interesting to note that, independent of all the non-linearities present, there appears a linear dependence of average fibre-stretch for each muscle group on the load for the described cases. From these figures it is apparent that both the gravitational orientation and pressure load have a significant effect on the stretch of the various muscle groups. In the supine case, for the most part muscles in tension under the influence of gravity remain so when the pressure load is increased, while for the upright case numerous muscle groups switch tensile states or attain a neutral state. In particular, the components of the genioglossus are overall in compression in the upright position, while in the supine configuration they are placed in tension. In both case application of a pressure load results in an increase in average stretch of the genioglossus muscles.
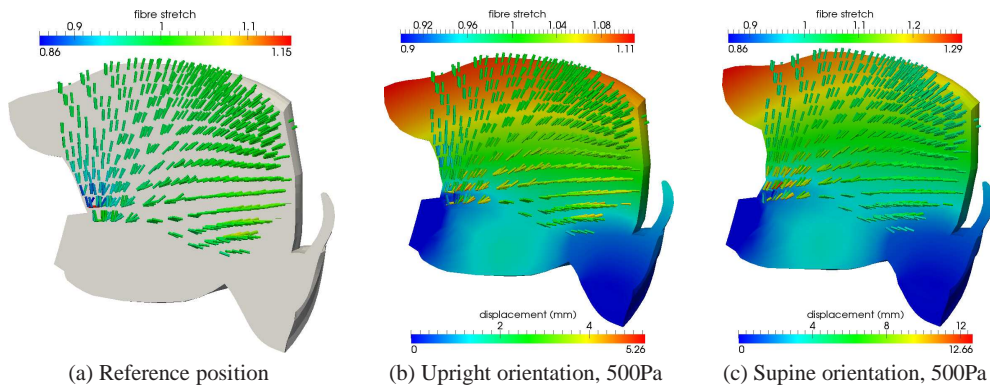
(a) Reference position   (b) Upright orientation, 500Pa   (c) Supine orientation, 500Pa

Figure 8. Passive tongue under the influence of gravity and pressure loading (displacement and genioglossus fibre stretch)

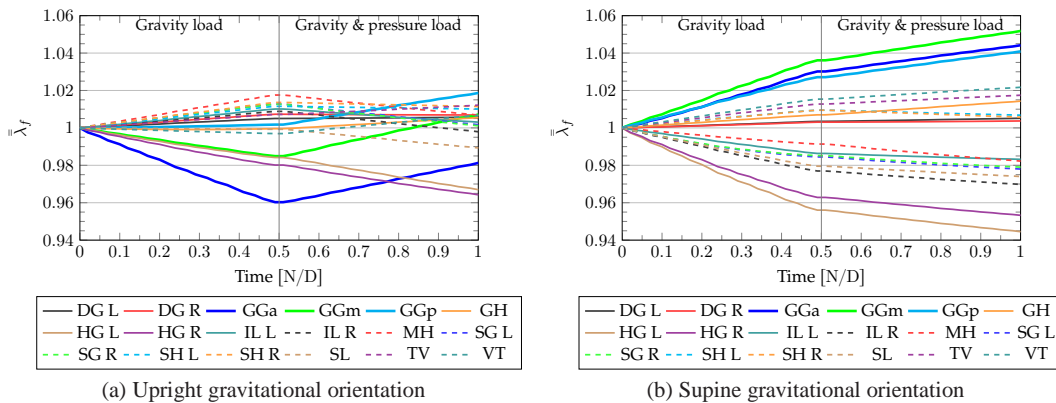(a) Upright gravitational orientation   (b) Supine gravitational orientation

Figure 9. Length-weighted average fibre stretches for muscles under different gravitational orientations

8.4. Individual muscle activation

Muscle groups are distributed in the tongue in such a way that the independent activation of each group results in a specific motion. The combination and interaction of the muscle groups gives the tongue great flexibility and the ability to perform complex yet precise motions. The following examples serve to illustrate that this muscle model coupled with an accurate geometry and histology dataset can produce realistic motions as described in literature.

The genioglossus depresses the tongue and pulls the tongue anteriorly for protrusion [20]. Figure 10a demonstrates this action. The anterior portion is pulled inferiorly and the posterior region is pulled forward towards the mandible. Since further geometric complexities such as the teeth have not been included, the action of the genioglossus in the confined space of the oral cavity has been exaggerated. However, it is demonstrated that contraction of this muscle contributes to the prevention of the tongue falling backwards into the posterior oropharyngeal region and thus its significance in preventing OSA.

The role of the styloglossus is to retract and draw the tongue upwards towards the palate [20]. Figure 10b demonstrates this action, as observed in the computational model. For the tongue to undergo more complex motions, the simultaneous activation of a number of muscle groups is
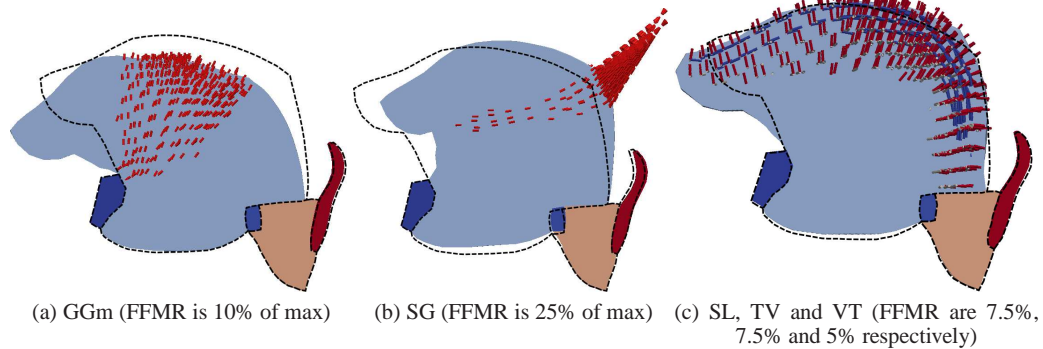
(a) GGm (FFMR is 10% of max) (b) SG (FFMR is 25% of max) (c) SL, TV and VT (FFMR are 7.5%, 7.5% and 5% respectively)

Figure 10. The final equilibrium state for individual activation (mid-saggital plane). The initial position before muscle contraction is indicated by dashed line.

required. For example, in order for the tongue to protrude out of the mouth, the transverse muscles (which narrow and elongate the tongue) and verticalis (which flattens and broadens the tongue) must both contract [20]. For this motion to be possible, the incompressible nature of the muscle matrix is exploited and the tongue is essentially squeezed out of the oral cavity. Figure 10c illustrates the simultaneous contraction of these two muscles in conjunction with the superior longitudinal, which is used to prevent the tongue tip of from curling downwards.

8.5. Position maintenance using neural control model

During respiration, ideally the tongue is held in a position that prevents blockage of the airway. This action is primarily performed by the genioglossus which, as is shown previously, is able to draw the tongue forward and downwards towards the mandible. We investigate the effectiveness of the neural model in terms of maintaining the original position of the tongue when the body is under the influence of gravity and a non-constant external load condition.

A sinusoidal load approximating three pressure loading cycles developed during breathing is applied to the surface of the tongue, epiglottis and supporting soft tissue. The pressure profile shape is described in (27). The maximum applied pressure of 350 Pa was the mean value of the range suggested to be developed in the airway [65]. Initial tests were performed to determine the effectiveness of the GA in comparison to a completely passive model. The passive model is used as a point of comparison as it indicates the limits of motion that could be expected under these conditions.

Figure 11 illustrates the effectiveness of the GA to control and minimise motion under temporally varying conditions. It was observed in the passive model that these markers experience a displacement history with a shape consistent with that of the applied loading. The displacement away from the reference condition varies with the gravitational orientation.

The position maintenance attributes of the GA formulation appear to be very good. Figure 11 demonstrates that under changing load the measured points on the tongue undergo minimal displacement away from their stable position, especially when compared to the maximum deflection observed in the passive model for the same applied load. For both gravitational loading orientations, the neural model ensures that the posterior surface point P_P undergoes a minimal displacement as the load varies. In both instances, the GA is able to select a group of muscles to contract that not

(a) Displacement of tongue posterior $\boldsymbol{P}_P$

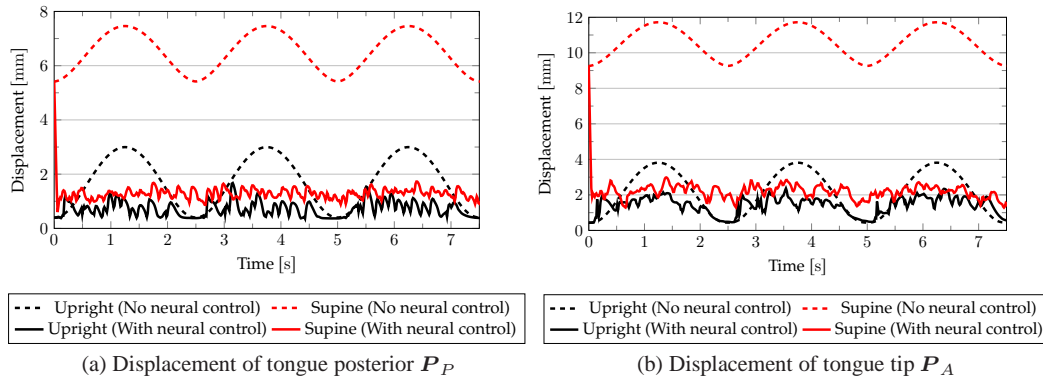(b) Displacement of tongue tip $\boldsymbol{P}_A$

Figure 11. Effect of orientation on tongue position with and without neural control. Refer to figure 7a for the position of the measurement points.

only moves it from its initial displacement due to gravitational loading alone (seen near $t = 0s$) but maintains this position under a time-varying load.

The natural equilibrium positions of the control points appear to be a small distance away from the desired reference position. This can be attributed to the chosen material and GA parameters, and the difficulty in the muscles attaining the required activation level to collectively satisfy the functional objective – the adjustment of muscle activation level at each time step is quite coarse. Figure 12 illustrates that the activation level does not change smoothly due to the choice of constant material parameters and the temporal resolution of the simulation. The same points explain the fluctuations observed in the position traces for all measured points.

In the supine case, the rear of the tongue at point $\boldsymbol{P}_P$ is maintained at an average of 1.29 mm away (in 3-d space) from the reference position. The deflection at this point due to changes in muscle activation is ± 0.16 mm from the mean, equating to a total displacement range of 0.32 mm away from the stable point. However, the position maintenance of the tongue tip $\boldsymbol{P}_A$ appears to be more difficult, with fluctuations of ± 0.30 mm from the stable average displacement of 2.20 mm. During upright orientation, point $\boldsymbol{P}_A$ has a displacement of 1.42 ± 0.39 mm, while $\boldsymbol{P}_P$ remains 0.72 ± 0.23 mm away from the reference position. In addition to the previous points regarding the muscle activation level, the high mean displacement away from the goal position may be further attributed to the muscle selection algorithm not selecting an antagonistic muscle pair to counteract the over-activation of certain muscle groups.

An account of the activation level history recorded for the medial part of the genioglossus is shown in figure 12a for both the upright and supine orientation under sinusoidal pressure loading. Comparison between this result and the experimentally recorded activation traces found in literature, namely [51, 52, 53], shows a good correlation in some key aspects. In both the experimental and computational recordings it was observed that:

1. muscle activation increases as the negative air pressure increases, and subsequently decreases as negative pressure decreases
2. the muscle response appears proportional to the air pressure (in this case, periodic) and occurs with minimal temporal delay, that is to say the response is nearly immediate
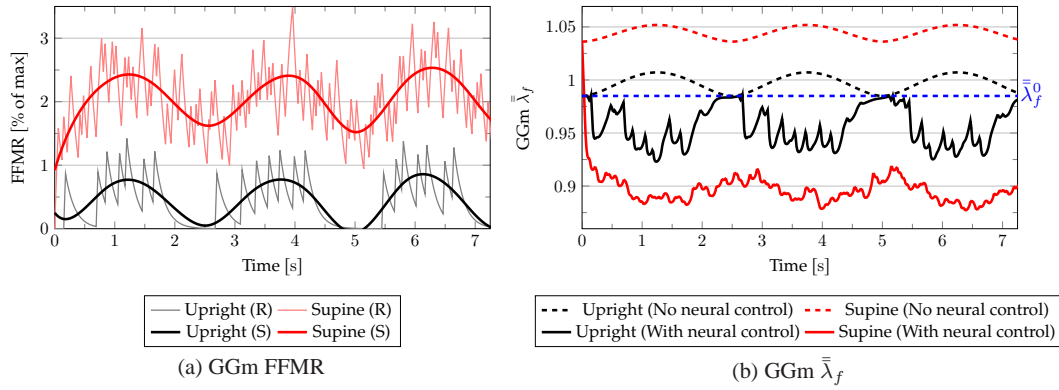3. the response is similar and repeatable for cyclic loading conditions.

Figure 12. Response of GGm to differing gravitational orientation. In 12a, raw data is shown as light lines and the data is fitted with a 12 coefficient B-Spline best-fit curve [66].

The differences in the response of the passive tissues described in section 8.3 explain the significantly different activation-level histories observed between the two gravitational orientations. For the case in which the body is in the upright position, gravity assists the genioglossus in preventing motion due to the applied load, resulting in a lower contractile force being required to resist motion. In the supine position, the genioglossus in order to prevent motion due to the action of both gravity and air pressure produces a greater contractile force. In both instances, however, the contractile response, is periodic and is in phase, but of different magnitude. It should be noted that, although the exact activation-level history is not repeated (due to the random nature of the GA), it is the variation between the FFMR trend for each load cycles that appears minimal. Additionally, the first cycle differs from subsequent cycles in that the level of activation in all muscles must first build up from zero when under full gravitational loading and increasing pressure loading. In subsequent cycles, the active muscle groups have attained an activation level sufficient to maintain the position of the tongue. In subsequent cycles for the supine case, the genioglossus remains active as a reaction to gravitational and other forces.

From figure 12b, we can draw a number of conclusions on the functioning of the genioglossus and aspects of the neural model. For both orientations, the genioglossus functions in the optimal contractile band ($f_c^L > 0.85$ as shown in figure 4a). However, it was observed that a greater contractile force was required during the breathing cycle for the supine case. This led to increased muscle shortening so that the muscle functions closer to the region of decreased contractile efficiency that occurs when $\lambda_c < 0.85$. Increased loading or muscle function deficiencies may cause the contractile element length to be reduced further and would rapidly lead to loss of contractile efficiency and possibly the inability to produce enough contractile force to counteract applied loads.

Additionally, assessment of the average fibre length for both cases suggests that monitoring the value of $\bar{\bar{\lambda}}_f$ and comparing it to the value at the zero-displacement configuration $\bar{\bar{\lambda}}_f^0$ is not necessarily a good indicator of whether activation of the muscle group will assist in returning the body to the reference configuration. Although figure 9 demonstrates that gravity and the airway pressure have the tendency to positively stretch the genioglossus, figure 12b shows that the average fibre stretch, by this measure, is well below the value recorded initially. The only reason it remains active is that the evaluation of this muscle groups is compulsory at all GA evaluation steps. This suggests that,

using this measure, the role of other muscle groups that may assist in position regulation are not evaluated by the GA and thus will remain passive.

8.5.1. Applied pressure

In the absence of muscle activation, an increase in negative airway pressure would result in increased deflection of the tongue surface. Figure 13 depicts the response of the genioglossus as the maximum nominal airway pressure is increased and decreased to the limits specified by [65].
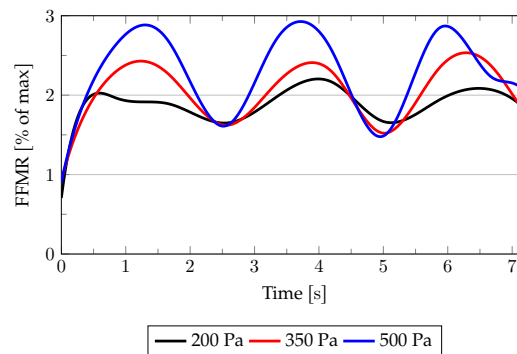

Figure 13. Effect of pressure magnitude on GGm FFMR

As expected, the scaling of the airway pressure results in a scaled response from the genioglossus. Increasing the negative airway pressure requires the GGm to produce a greater contractile force, seen here as increased muscle activity, in order for the tongue to maintain its position. The periodic contractile response of the GGm is more apparent as the pressure decreases. The response shown here further reinforces the idea that the genioglossus is indeed the main airway dilator muscle responsible for the maintenance of airway patency. Under all situations, removal of the pressure load reduces the genioglossus activation level to the same value, namely that required to resist gravity.

9. CONCLUSIONS

We have discussed the development of an anatomically and histologically accurate model of the tongue and associated tissues. Physiologically sound models, with parameters derived from experimental data, have been used to simulate the constitutive behaviours of tissues. The muscle model incorporated into the framework is representative of both active and passive skeletal muscle and is shown to reproduce recognisably realistic movement in the tongue.

In the absence of meaningful experimental control-data, a neural model has been developed in an attempt to replicate the physiological stimulation of muscle groups. The criterion on which the choice of muscle activation is based is derived from a physiological viewpoint. Under loading similar to that experienced during breathing, the model has been shown to produce a response for the genioglossus that compares favourably to that measured in experimental procedures. Further, it has also been demonstrated that intuitively correct responses of the genioglossus under changing conditions, posture, gravitation and so forth, are able to be displayed.

Further research should include the exploration of inertial effects, a refinement of the neural model, and a holistic representation of the entire upper-airway physiology. These refinements would allow the model to reproduce even more accurately the conditions experienced during physiologically normal phonetics and pathological states such as sleep apnoea, towards gaining a better understanding of these phenomena.

10. ACKNOWLEDGEMENTS

REFERENCES

1. Wilhelms-Tricario R. Physiological modeling of speech production: Methods for modeling soft-tissue articulators. *Journal of the Acoustical Society of America* 1995; **97**:3085–3098.
2. Sanguineti V, Laboissiere R, Ostry D. A dynamic biomechanical model for neural control of speech production. *Journal of the Acoustical Society of America* 1998; **103**:1615–1627.
3. Fang Q, Fujita S, Lu X, Dang J. A model-based investigation of activations of the tongue muscles in vowel production. *Acoustical Science and Technology* 2009; **30**:277–287.
4. Gerard JM, Wilhelms-Tricarico R, Perrier P, Payan Y. A 3d dynamical biomechanical tongue model to study speech motor control. *Recent Research Developments in Biomechanics* 2003; **1**:49–63.
5. Vogt F, Lloyd JE, Buchaillard S, Perrier P, Chabanas M, Payan Y, Fels SS. Efficient 3d finite element modeling of a muscle-activated tongue. *ISBMS 06*, 2006; 19–28.
6. Wu MC, Han JC, Röhrle O, Thorpe W, Nielsen P. Using three-dimensional finite element models and principles of active muscle contraction to analyse the movement of the tongue. *11th Australian International Conference on Speech Science & Technology*, 2006; 354–359.
7. Buchaillard S, Perrier P. A biomechanical model of cardinal vowel production: Muscle activations and the impact of gravity on tongue positioning. *Acoustical Society of America* 2009; **126**:2033–2051.
8. Stavness I, Lloyd JE, Payan Y, Fels S. Coupled hard-soft tissue simulation with contact and constraints applied to jaw-tongue-hyoid dynamics. *International Journal for Numerical Methods in Engineering* 2011; **27**:367–390.
9. Huang Y, Malhotra A, White DP. Computational simulation of human upper airway collapse using a pressure-/state-dependent model of genioglossal muscle contraction under laminar flow conditions. *J Appl Physiol* Sep 2005; **99**(3):1138–1148. URL http://jap.physiology.org/cgi/content/abstract/99/3/1138.
10. Huang Y, White DP, Malhotra A. Use of computational modeling to predict responses to upper airway surgery in obstructive sleep apnea. *Laryngoscope* 2007; **117**:648–653.
11. Fujita S, Dang J, Suzuki N, Honda K. A computational tongue model and its clinical application. *Oral Science International* 2007; **109**:97–109.
12. Martins JAC, Pires EB, Salvado R, Dinis PB. A numerical model of passive and active behaviour of skeletal muscles. *Computer Methods in Applied Mechanics and Engineering* 1998; **151**:419–433.
13. Martins JAC, Pato MPM, Pires EB. A finite element model of skeletal muscles. *Virtual and Physical Prototyping* September 2006; **1**(1):159–170.
14. Herzog W, Ait-Haddou R. Considerations on muscle contraction. *Journal of Electromyography and Kinesiology* 2002; **12**:425–433.
15. Lieber RL. *Skeletal Muscle Structure, Function and Plasticity: The Physiological Basis of Rehabilitation*. Lippincott, Williams and Wilkins, 2002.
16. US National Library of Medicine. The Visible Human Project Ⓡ. http://www.nlm.nih.gov/research/visible/visible_human.html August 2009. URL http://www.nlm.nih.gov/research/visible/visible_human.html.

17. Materialise. http://www.materialise.com/mimics 2010.

18. Davies D ((ed.)). *Gray's Anatomy*. 34th edn., Longmans, Green & Co Ltd., 1967.

19. Mortley ME. *The Development and Disorders of Speech in Childhood* . Third edn., Churchhill Livingstone, 1972.

20. Agur AMR, Dalley AF. *Grant's Atlas of Anatomy*. 11 edn., Lippincott Williams & Wilkins, 2005.

21. Ansys. http://www.ansys.com/products/icemcfd.asp 2010.

22. Miyawaki K, Hirose H, Ushijima T, Sawashima M. A preliminary report on the electromyographic study of the activity of lingual muscles. *Annual Bulletin RILP* 1975; **9**:91–106.

23. Dang J, Honda K. A physiological articulatory model for simulating speech production process. *Acoustical Science and Technology* 2001; **22**:415–425.

24. Humphrey JD, Yin FCP. On constitutive relations and finite deformations of passive cardiac tissue: I. a pseudostrain-energy function. *Journal of Biomechanical Engineering* 1987; **109**:298–304.

25. Holtzapfel GA, Gasser TC, Ogden RW. A new constitutive framework for arterial wall mechanics and a comparative study of material models. *Journal of Elasticity* 2000; **61**:1–48.

26. Baaijens F, Bouten C, Driessen N. Modeling collagen remodeling. *Journal of Biomechanics* 2010; **43**:166–175.

27. Planas J, Guinea GV, Elices M. Constitutive model for fiber-reinforced materials with deformable matrices. *Physical Review E - Statistical, Nonlinear and Soft Matter Physics* 2007; **76**:041 903.

28. van Oijen CHGA. Mechanics and design of fiber-reinforced vascular prostheses. PhD Thesis, Technische Universiteit Eindhoven 2003.

29. Van Ee CA, Chasse AL, Myers BS. Quantifying skeletal muscle properties in cadaveric test specimens: Effects of mechanical loading, postmortem time, and freezer storage. *Journal of Biomechanical Engineering* 2000; **122**:9–14.

30. Van Loocke M, Lyons CG, Simms CK. A validated model of passive muscle in compression. *Journal of Biomechanics* 2006; **39**:2999–3009.

31. Simo JC, Taylor RL. Quasi-incompressible finite elasticity in principal stretches. Continuum basis and numerical algorithms. *Computer Methods in Applied Mechanics and Engineering* 1991; **85**:273–310.

32. Miehe C. Aspects of the formulation and finite strain element inplementation of large strain isotropic elasticity. *International Journal for Numerical Methods in Engineering* 1994; **37**:1981–2004.

33. Nagtegaal JC, Parks DM, Rice JR. On numerically accurate finite element solutions in the fully plastic range. *Computer Methods in Applied Mechanics and Engineering* 1974; **4**:153–177.

34. Simo JC, Taylor RL, Pister KS. Variational and projection methods for the volume constraint in finite deformation elasto-plasticity. *Computer Methods in Applied Mechanics and Engineering* 1985; **51**:177–208.

35. Bangerth W, Hartmann R, Kanschat G. deal.II — a general-purpose object-oriented finite element library. *ACM Transactions on Mathematical Software* 2007; **33**(4), doi:10.1145/1268776.1268779. Article 24, 27 pages.

36. Bangerth W, Kanschat G. deal.II *Differential Equations Analysis Library, Technical Reference* 2011. URL http://www.dealii.org, http://www.dealii.org.

37. Miller-Young JE, Duncan NA, Baroud G. Material properties of the human calcaneal fat pad in compression: experiment and theory. *Journal of Biomechanics* 2002; **35**:1523–1531.

38. Perrier P, Payan Y, Zandipour M, Perkell J. Influences of tongue biomechanics on speech movements during the production of velar stop consonants: A modeling study. *Journal of the Acoustical Society of America* 2003; **114**:1582–1599.

39. Dang J, Honda K. Construction and control of a physiological articulatory model. *Journal of the Acoustical Society of America* 2004; **115**:853–870.

40. Fung YC. *Biomechanics: Mechanical Properties of Living Tissues Second Edition*. Springer, 1993.

41. Abd-El-Malek S. Observations on the morphology of the human tongue. *Journal of Anatomy* 1939; **73**:201–210.

42. Takemoto H. Morphological analyses of the human tongue musculature for three-dimensional modeling. *Journal of Speech, Language, and Hearing Research* 2001; **44**:95–107.

43. Lieber RL, Runesson E, Einarsson F, Friden J. Inferior mechanical properties of spastic muscle bundles due to hypertrophic but compromised extracellular matrix material. *Muscle Nerve* 2003; **28**:464–471.

44. Humbert IA, Reeder SB, Porcaro EJ, Kays SA, Brittain JH, Robbins J. Simultaneous estimation of tongue volume and fat fraction using ideal-fse. *Journal of Magnetic Resonance Imaging* 2008; **28**:504–508.

45. Miller JL, Watkin KL, Chen MY. Muscle, adipose, and connective tissue variations in intrinsic musculature of the adult human tongue. *Journal of Speech, Language, and Hearing Research* 2002; **45**:51–65.

46. Press W, Teukolsky S, Vetterling W, Flannery B. *Numerical Recipies: The Art of Scientific Computing*. 3 edn., Cambridge University Press, 2007.

47. Hill AV. The mechanics of active muscle. *Proceedings of the Royal Society of London. Series B.* 1953; **141**:104–117.

48. Hill AV. The heat of shortening and the dynamic constants of muscle. *Proceedings of the Royal Society of London, Series B* 1938; **126**:136–195.

49. Johansson T, Meier P, Blickhan R. A finite-element model for the mechanical analysis of skeletal muscles. *Journal of Theoretical Biology* 2000; **206**:131–149.

50. Pandy MG, Zajac FE, Sim E, Levine WS. An optimal control model for maximum-height human jumping. *Journal of Biomechanics* 1990; **23**:1185–1198.

51. Malhotra A, Pillar G, Fogel RB, Beauregard J, Edwards JK, Slamowitz DI, Shea SA, White DP. Genioglossal but not palatal muscle activity relates closely to pharyngeal pressure. *American Journal of Respiratory and Critical Care Medicine* 2000; **162**:10581062.

52. Stanchina ML, Malhotra A, Fogel RB, Ayas N, Edwards JK, Schory K, White DP. Genioglossus muscle responsiveness to chemical and mechanical stimuli during nonrapid eye movement sleep. *American Journal of Respiratory and Critical Care Medicine* 2002; **165**:945–949.

53. Pierce R, White D, Malhotra A, Edwards J, Kleverlaan D, Palmer L, Trinder J. Upper airway collapsibility, dilator muscle activation and resistance in sleep apnoea. *European Respiratory Journal* 2007; :345–353.

54. Bailey EF. Activities of human genioglossus motor units. *Respiratory Physiology & Neurobiology* 2011; **179**:14–22, doi:10.1016/j.resp.2011.04.018.

55. Cheng S, Butler JE, Gandevia SC, Bilston LE. Movement of the tongue during normal breathing in awake healthy humans. *The Journal of Physiology* 2008; **586**:4283–4294.

56. Mitchell M. *An Introduction to Genetic Algorithms*. MIT Press, 1999.

57. Whitley D. A genetic algorithm tutorial. *Statistics and Computing* 1994; **4**:65–85.

58. Wall M. GAlib: A C++ Library of Genetic Algorithm Components July 2010. URL http://lancet.mit.edu/ga/, version 2.4.7.

59. Peterson D, Bronzino J. *Biomechanics: Principles and Applications*. CRC Press, 2008.

60. Reilly DT, Burstein AH. The mechanical properties of cortical bone. *The Journal of Bone and Joint Surgery* 1974; **56**:1001–1022.

61. Li LP, Soulhat J, Buschmann MD, Shirazi-Adl A. Nonlinear analysis of cartilage in unconfined ramp compression using a fibril reinforced poroelastic model. *Clinical Biomechanics* 1999; **14**:673–682.

62. Erdemir A, Viveiros ML, Ulbrecht JS, Cavanagh PR. An inverse finite-element model of heel-pad indentation. *Journal of Biomechanics* 2006; **39**:1279–1286.

63. Farvid MS, Ng TW, Chan DC, Barrett PH, Watts GF. Association of adiponectin and resistin with adipose tissue compartments, insulin resistance and dyslipidaemia. *Diabetes, Obesity and Metabolism* 2005; **7**:406–413.

64. Gee MW, Forster C, Wall WA. A computational strategy for prestressing patient-specific biomechanical problems under finite deformation. *International Journal for Numerical Methods in Engineering* 2010; **26**:52–72.

65. Van Hirtum A, Chouly F, Teul A, Payan X Yand Pelorson. In-vitro study of pharyngeal pressure losses at the origin of obstructive sleep apnea. *Engineering in Medicine and Biology Society, 2003. Proceedings of the 25th Annual International Conference of the IEEE*, 2004.

66. Galassi M, Davies J, Theiler J, Gough B, Jungman G, Alken P, Booth M, Rossi F. *GNU Scientific Library Reference Manual*. Third edn., Network Theory Ltd, 2010. URL http://www.gnu.org/software/gsl/.